Supporting information

Single-atom mediated crystal facet engineering for the exceptional production of acetate in CO electrolysis

Jiacheng Liu[†a], Yan Wen[†a], Wei Yan[†a], Zhongliang Huang[†a], Xiaozhi Liu[b], Xuan Huang[a], Changhong Zhan[a], Yuqi Zhang[a], Wei-Hsiang Huang[c], Chih-Wen Pao[c], Zhiwei Hu[d], Dong Su[b], Shunji Xie [a,f], Ye Wang [a,f], Jiajia Han[e*], Haifeng Xiong[a,f*], Xiaoqing Huang[a,f*], and Nanjun Chen[a,f*]

[a] State Key Laboratory of Physical Chemistry of Solid Surfaces, College of Chemistry and Chemical Engineering, Xiamen University, Xiamen, 361005, China.

[b] Beijing National Laboratory for Condensed Matter Physics, Institute of Physics, Chinese Academy of Sciences, Beijing 100190, China.

[c] National Synchrotron Radiation Research Center, 101 Hsin-Ann Road, Hsinchu 30076, Taiwan.

[d] College of Chemistry, Max Planck Institute for Chemical Physics of Solids, Dresden 01187, Germany.

[e] State Key Lab of Physical Chemistry of Solid Surfaces, College of Materials, Xiamen University, Xiamen 361005, China.

[f] Innovation Laboratory for Sciences and Technologies of Energy Materials of Fujian Province (IKKEM), Xiamen, 361005, China.

[*]E-mail: jiajiahan@xmu.edu.cn; haifengxiong@xmu.edu.cn; hxq006@xmu.edu.cn;

nanjun.chen@xmu.edu.cn

METHODS

Chemicals. Cu(II) acetylacetonate ($Cu(acac)_2$), Cu(II) nitrate trihydrate ($Cu(NO_3)_2 \cdot 3H_2O$), Co(II) acetylacetonate ($Co(acac)_2$), l-ascorbic acid ($C_6H_8O_6$, AA), phloroglucinol anhydrous ($C_6H_6O_3$), Nafion (5%) and oleylamine ($C_{18}H_{37}N$, OAm) were supplied from Aladdin. Co(II) chloride hexahydrate ($CoCl_2 \cdot 6H_2O$, 99%), hexamethylenetetramine ($C_6H_{12}N_4$, HMTA), hexadecyltrimethylammonium bromide ($C_{19}H_{42}BrN$, CTAB), and cyclohexane (C_6H_{12}, 85%) were purchased from SCR. All chemicals were used as received without further purification. The water (18 MΩ cm^{-1}) used in all experiments was collected by passing through an ultrapure purification system (Aqua Solutions).

Synthesis of $CuCo_1$ sheets, $CuCo_1$ crystals, and Cu crystals. In a typical synthesis of $CuCo_1$ sheets, 12 mg $Cu(acac)_2$, 20 mg $CoCl_2 \cdot 6H_2O$, 27 mg CTAB, 72 mg $C_6H_6O_3$, and 5 mL OAm were added into a vial (30 mL). The vial is capped and sonicated until the solution changes from a blue suspension to a homogeneous black solution. Then the solution was heated from room temperature to 220 °C within 30 minutes and kept at 220 °C for 5 h in an oil bath. The resulting products were collected by centrifugation and washed five times with a cyclohexane/ethanol mixture. Preparation of $CuCo_1$ crystals and Cu crystals was similarly conducted, but without the addition of CTAB and without the addition of cobalt(II) chloride hexahydrate.

Synthesis of $CuCo_{NPs}$ Sheets. In a typical synthesis of $CuCo_{NPs}$ sheets. Firstly, we synthesized the Cu triangle from the previous literature.[1] Then, 10 mg Cu sheets, 10 mg $Co(acac)_2$, 30mg AA, and 5 mL OAm were added into a vial (30 mL). The vial is capped and sonicated. Then the solution was heated from room temperature to 220 °C within 30 minutes and kept at 220 °C for 5 h in an oil bath. The resulting products were collected by centrifugation and washed five times with a cyclohexane/ethanol mixture.

Characterizations. The morphology of the synthesized sample was first characterized by a low-magnification transmission electron microscope (TEM, JEM-1400, 100 kV). A FEI Tecnai F20 TEM (200 kV) was employed to achieve the HAADF-STEM images, high-magnification TEM images, and EDS line scan/mapping. AC-HAADF-STEM was tested on FEI Titan Cubed Themis G2300. An energy dispersive X-ray spectrometer coupled with a Zeiss scanning electron microscope was used to acquire the chemical composition. The XRD pattern was measured on a SmartLab-SE powder diffractometer with a Cu radiation source ($\lambda = 0.15406$ nm). An SSI S-Probe XPS spectrometer was employed to acquire the surface chemical information. The XAS spectra were acquired at the TPS44A and the TLS01C1 beamline of the National Synchrotron Radiation Research Center (NSRRC, Hsinchu, Taiwan). The data were processed according to standard procedures using the software of the Demeter program package (Version 0.9.24).

CORR test in flow cell. CORR test was carried out in a flow cell that consisted of two electrolyte chambers (20 × 5 × 3, mm) and one gas chamber (20 × 5 × 5, mm). An anion exchange membrane (Fumasep-FAA-3-PK-130) was placed between two electrolyte chambers to separate the anode and cathode. Catalyst-deposited gas diffusion electrode (GDE), micro Ag/AgCl electrode (4.0 M KCl), and platinum sheet (0.5 mm thickness) were used as the working electrode, reference electrode, and anode, respectively. To fabricate the working electrode, 3 mg of catalysts were dispersed in 1 mL of cyclohexane with 20 μL of 5 wt% Nafion solution to prepare a catalyst slurry, and then the slurry was sprayed onto a carbon paper (Sinero, YLS-30T). The loading amount of catalysts on GDE was controlled to ~0.44 mg

cm^{-2}. The working electrode was placed between gas and catholyte chambers to ensure gaseous CO diffusion and reaction at the catholyte/catalysts interface. The referencethe electrodes were inserted in catholyte chamber and maintained at a specified distance with the working electrode. An electrochemical workstation (CHI660, Chenhua, Shanghai) with a current amplifier was used to perform the CORR test. 1 M KOH (20 mL) was circulated through the electrolyte chambers under constant flow (20 mL min^{-1}) via peristaltic pump. CO was supplied into gas chambers by a mass-flow controller at a constant flow rate of 30 mL min^{-1}. Reactions were tested via chronopotentiometry at differing currents for 0.5 h without iR correction. Gas and liquid products were analyzed via GC (Agilent 8890) and ^{1}H NMR (Bruker AVANCE III HD 500MHz), respectively.

The Potentials were referenced to RHE and iR correction performed based on the following equation:

$$E_{RHE} = E_{vs\ Ag/AgCl} + 0.059 \times pH + 0.21 \quad (1)$$

FE for the formation of CORR product was computed by the following equation:

$$FE = \frac{nZF}{Q} = \frac{nZF}{I \times t} \quad (2)$$

The formation rate (R) for each species was calculated using the following equation:

$$R = \frac{Q \times FE}{96485 \times Z \times t \times S} \quad (3)$$

Where Z is the number of transferred electrons for each product, F denotes the Faradaic constant, Q is the charge, I represents the applied current, t is the reaction time, n is the total product, and S denotes the geometric area of the electrode (cm^2).

CORR test in MEA. Electroreduction of CO in MEA consisted of two titanium backplates (TA2 grade) with a 4.0 cm^{-2} serpentine flow field, and MEA. Catalyst-deposited GDE (~0.44 mg cm^{-2}) and IrO_2 (0.5 mm thickness) were used as the cathode and anode, respectively. The cathode and anode were pressed onto sides of anion exchange membrane (Sustainion X37-50-grade 60, Dioxide Materials). The gap between the electrodes was minimized to reduce ohmic loss. Gaseous CO (30 mL min^{-1}) was passed behind the GDL to contact the catalyst, and 2 M KOH was used as the anolyte which was circulated via pump at 20 mL min^{-1}. CORR performance for MEA was evaluated by applying different currents with a current amplifier in the two-electrode system at the CHI660 (Chenhua, Shanghai) electrochemical workstation. Cathodic gas products were vented through a simplified cold-trap to collect permeable liquid prior to gas chromatograph testing. FE values for the liquid products were computed based on the total mass of product collected on anode and cathode.

ECSA measurement. ECSA was determined by the double-layer capacitance in an H-cell. The area of the electrode for the calculation of current density is 0.196 cm^2. Specifically, cyclic voltammetry (CV) scans were conducted at the potential range from 0.836 to 0.936 V *vs*. RHE with increasing scan rates of 10, 20, 40, 60, 80, and 100 mV s^{-1}. The capacitance currents at 0.886 V *vs*. RHE were plotted against scan rates, and the double-layer capacitance (C_{dl}, mF cm^{-2}) was derived from the slope according to the following Equation (4):

$$C_{dl} = \frac{I}{v} \quad (4)$$

where I is the capacitance current (half of the difference between the anodic current density (J_a) and cathodic current density (J_c), (J_a-J_c)/2), and v is the scan rate.
Specifically, ECSA can be calculated by the following formula:

$$ECSA = \frac{C_{dl}}{C_s} \times S \quad (5)$$

where S is the geometric area of the electrode, and Cs denotes the empirical capacitance value of 29 μF cm^{-2} for planar polycrystalline Cu.

***In situ* ATR-SEIRAS measurement.** *In situ* ATR-SEIRAS[2] was employed to trace the signals of the intermediates using a Nicolet Nexus 6700 Spectroscopy equipped with a liquid nitrogen-cooled mercury-cadmium-telluride (MCT) detector. An ECIR-II cell equipped with a Pike Veemax III ATR in a three-electrode system was provided from Shanghai Linglu Instrument & Equipment Co. To improve the signal intensity, the monocrystal silicon was initially coated with a layer of Au using the chemical plating method. Then, 20 μL catalyst ink was dropped on the surface of the Au film, which served as the working electrode. Platinum sheet and Ag/AgCl electrode were used as counter electrodes and reference electrodes, respectively. Before the test, the CO feeding gas was purged into the electrolyte for 30 minutes and continuously bubbled during the measurement. The potential-dependent *in situ* ATR-SEIRAS tests were carried out with LSV test from 0 V to –0.7 V (*vs*. RHE) with a scan rate of 5 mV s^{-1}. The reference spectrum was taken at 0.1 V. The resulting spectra are reported as a relative change in reflectivity ($\frac{\triangle R}{R}$) based on the recent publication,[40] which can be calculated according to Equation 5.

$$\frac{\triangle R}{R} = \frac{R(E_s) - R(E_R)}{R(E_R)} \quad (6)$$

where $R(E_R)$ and $R(E_S)$ denote the reflectivity at the reference and the sample potentials, respectively.

Theoretical calculations. The calculations for this study were conducted by using density functional theory (DFT) as implemented in the Vienna Ab initio Simulation Package (VASP).[3] The interactions between ions and electrons were described using the projector-augmented wave method (PAW).[4] The valence electrons were considered using a plane wave basis set with an energy cut-off of 520 eV, which ensured accurate total energy calculations. The exchange-correlation energy of the interacting electrons was determined using the Perdew-Burke-Ernzerhof (PBE) functionals within the generalized gradient approximation (GGA).[5, 6] The electronic convergence criterion was set to 10^{-6} eV, and the ionic convergence criterion was set to 10^{-2} eV $Å^{-1}$. The van der Waals interaction was included using Grimme's scheme (DFT-D3).[7] The graphene substrate model consisted of a 4×4×1 supercell with a vacuum gap of 15 Å. For structural optimizations, a 3×3×1 Monkhorst-Pack grid centered on the Gamma point was used to sample the Brillouin zone, while a 4×4×1 grid was used for static calculations. The adsorption energies relevant to the possible stable configuration of the CORR intermediate products, such as *CO-CO, *CO-

COH, *COH-COH, *C-CO, *CH-CO, *CH_2-CO and CH_3-COOH, were used to construct free energy diagrams, which is calculated as:

$$E_{ads} = E_{total} - E_{slab} - E_{adsorbate} \quad (7)$$

where E_{ads} is the total energy of the system with the adsorbate bound to the substrate (e.g., CO on Cu(111)Co_1), E_{slab} is the energy of the clean substrate (e.g., Cu(111)Co_1), and $E_{adsorbate}$ is the energy of the isolated adsorbate in its equilibrium state.

The Gibbs free energies of these molecules as a result of electrochemical adsorption reactions are calculated using the following equation:

$$\Delta G = \Delta E_{tot} + \Delta E_{ZPE} - T\Delta S \quad (8)$$

where ΔE_{tot} is the change in total energy obtained from DFT, ΔE_{ZPE} and ΔS are the changes in zero-point energy and entropy at standard conditions.

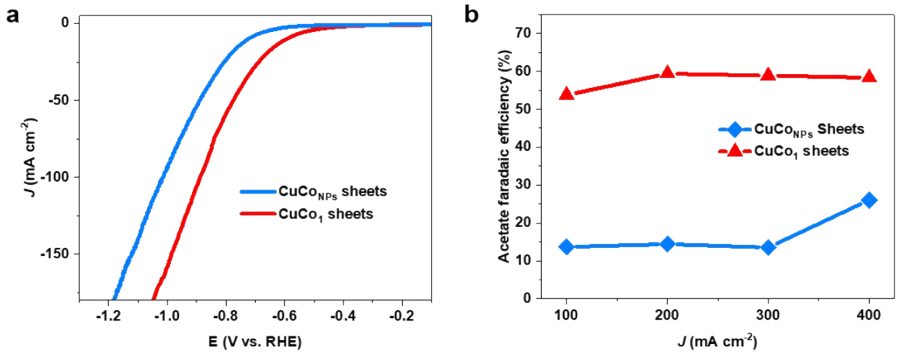

Fig. S1. (a) Liner sweep voltammetry curves toward CORR for $CuCo_{NPs}$ sheets and $CuCo_1$ sheets. (b) Acetate Faradaic efficiency at different current densities of $CuCo_{NPs}$ sheets and $CuCo_1$ sheets in a flow cell.

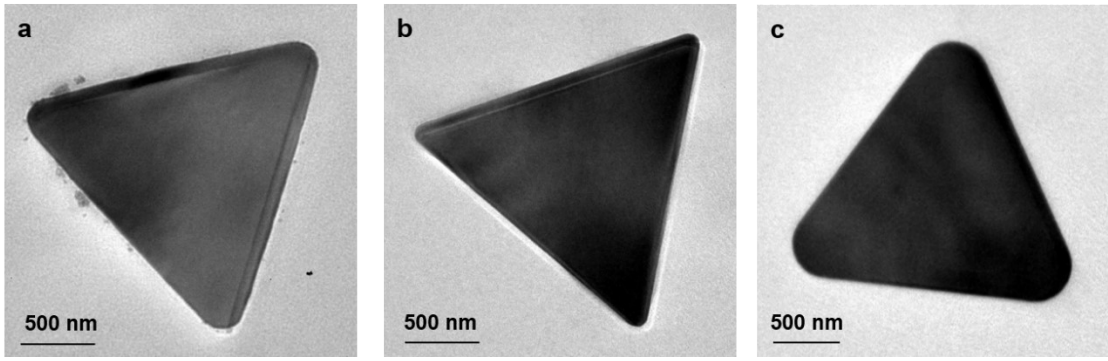

Fig. S2 TEM images of $CuCo_1$ sheets with a cobalt content of about (a) 3%, (b) 5%, and (c) 8%.

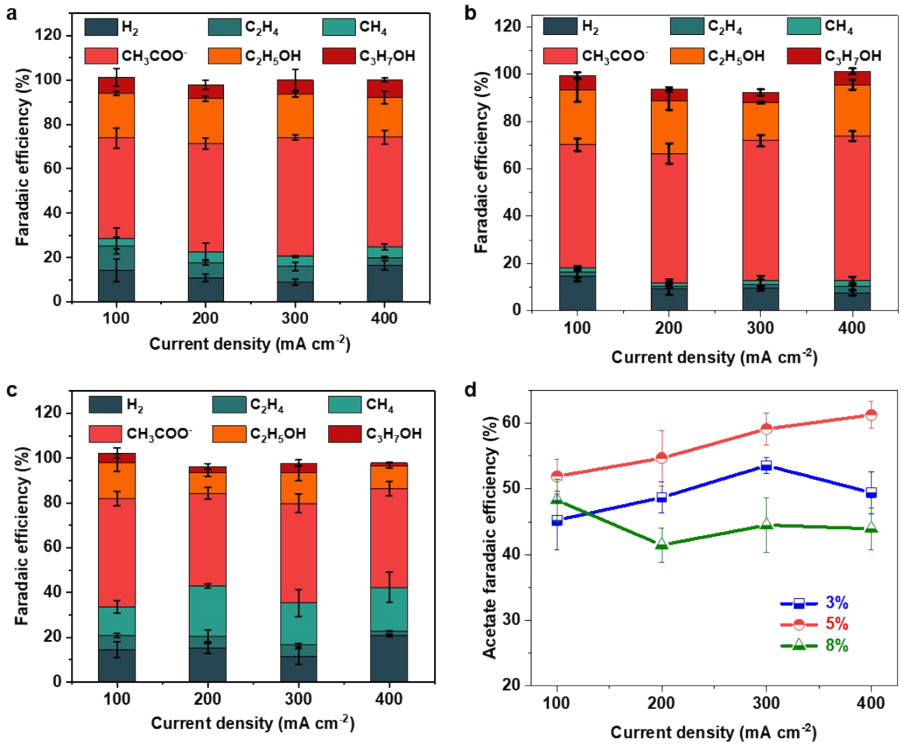

Fig. S3 FEs of all CORR products at different current densities of $CuCo_1$ sheets with a cobalt content of about (a) 3%, (b) 5%, and (c) 8%. (d) Comparison of acetate faradaic efficiency over $CuCo_1$ sheets with a cobalt content of about 3%, 5%, and 8%.

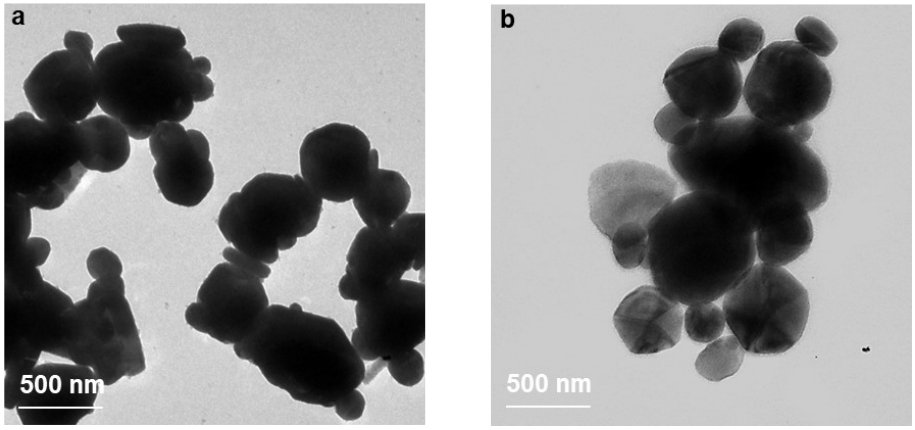

Fig. S4 TEM images of (a, b) $CuCo_1$ crystals.

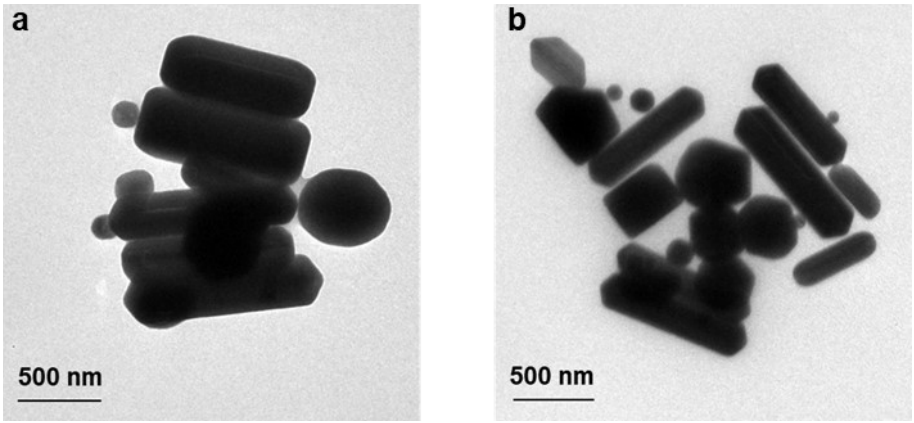

Fig. S5 TEM images of (a, b) Cu crystals.

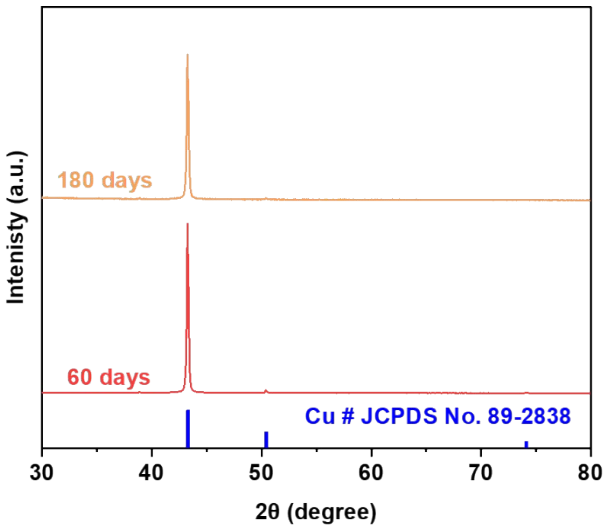

Fig. S6 XRD patterns of $CuCo_1$ sheets after being exposed to air at room temperature for 60 days and 180 days.

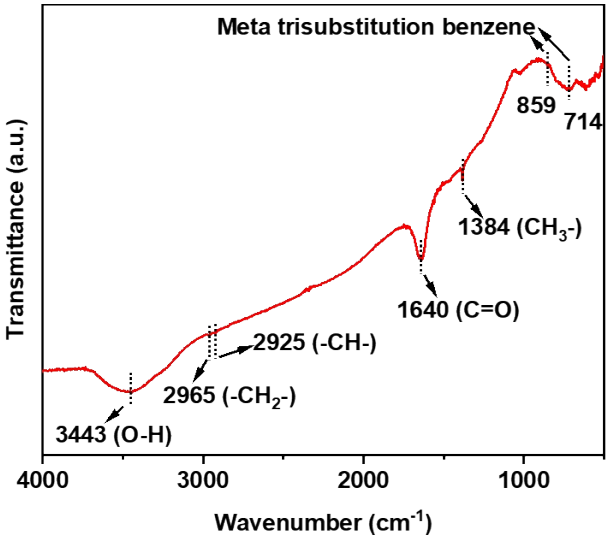

Fig. S7 Infrared spectrum of $CuCo_1$ sheets.

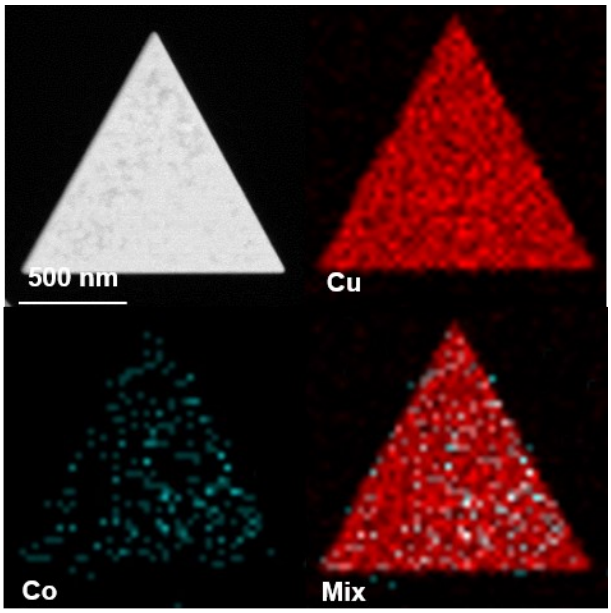

Fig. S8 HAADF-STEM image with elemental mappings of $CuCo_1$ sheets.

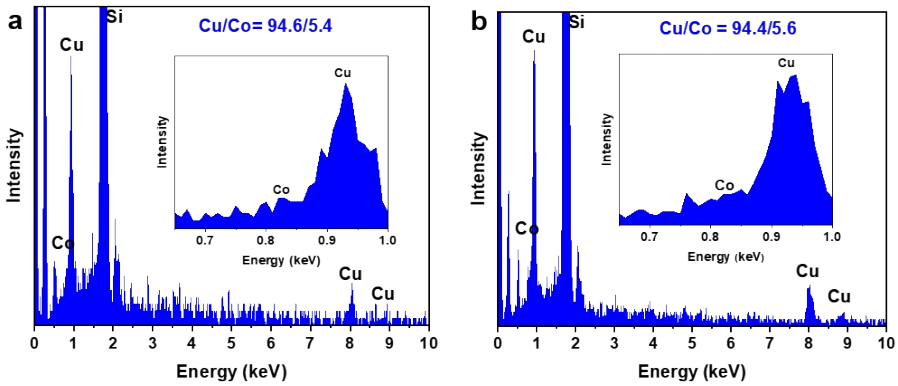

Fig. S9 SEM-EDS spectra of (a) $CuCo_1$ sheets and (b) $CuCo_1$ crystals.

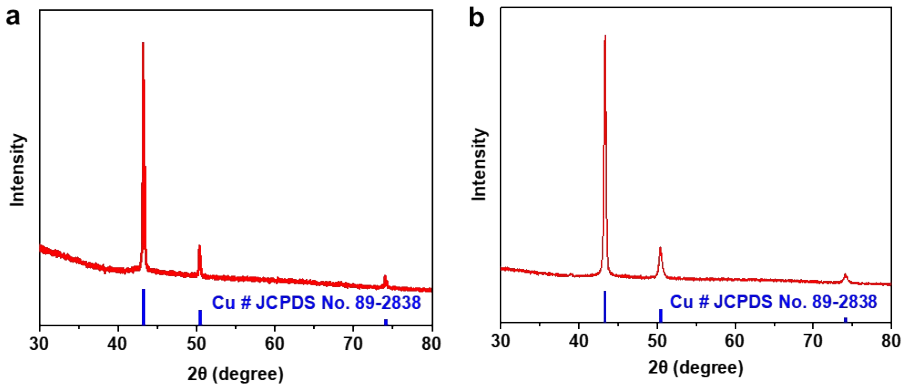

Fig. S10 XRD patterns of (a) $CuCo_1$ crystals and (b) Cu crystals.

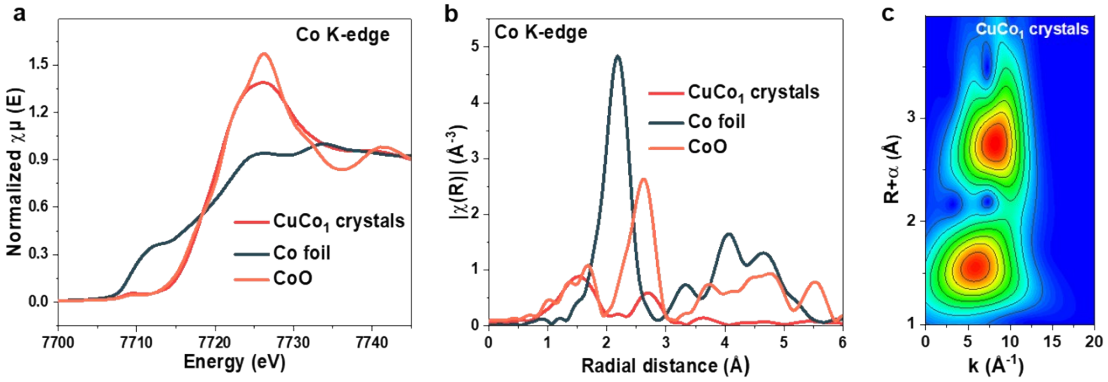

Fig. S11 (a) Co K-edge XANES and (b) Fourier transform EXAFS spectra of $CuCo_1$ crystals, Co foil, and CoO. (c) Wavelet transformation of $CuCo_1$ crystals.

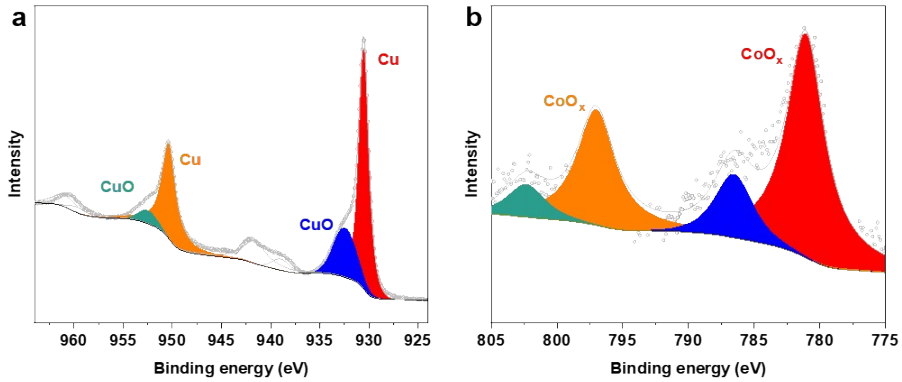

Fig. S12 (a) Cu 2p XPS and (b) Co 2p XPS spectra of $CuCo_1$ crystals.

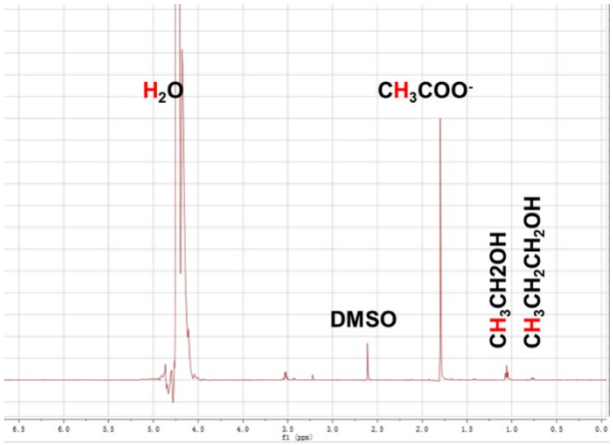

Fig. S13 ^{1}H-NMR spectrum of the electrolyte to analyze the liquid products after CO electroreduction over $CuCo_1$ sheets in a flow cell.

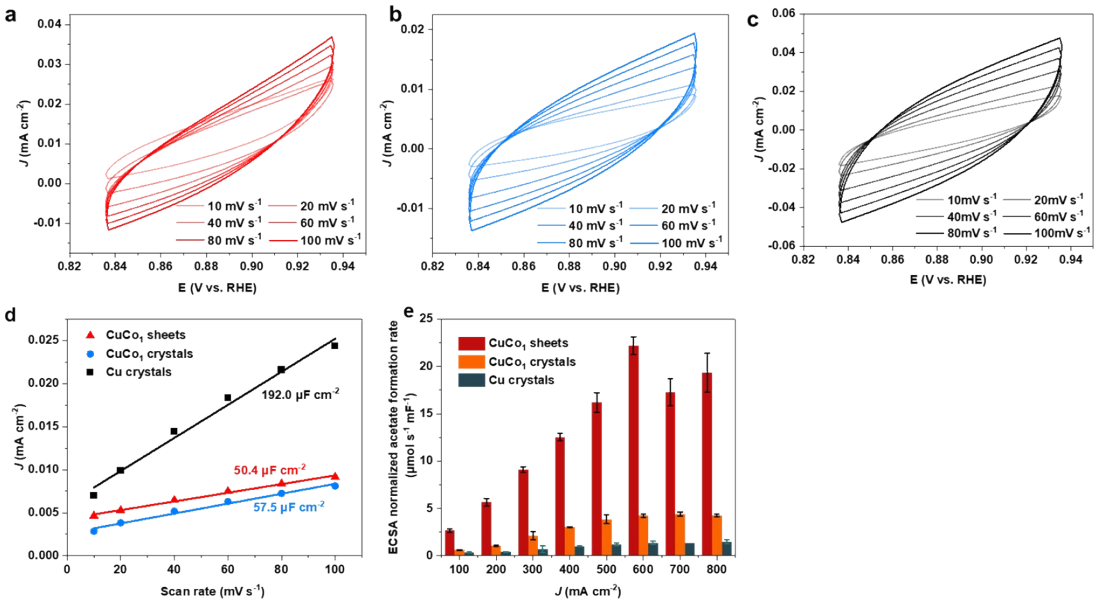

Fig. S14 Electrochemically active surface area measurements of (a) $CuCo_1$ sheets, (b) $CuCo_1$ crystals, and (c) Cu crystals. (d) Double-layer capacitance of $CuCo_1$ sheets, $CuCo_1$ crystals, and Cu crystals. (e) ECSA normalized acetate formation rates of $CuCo_1$ sheets, $CuCo_1$ crystals, and Cu crystals.

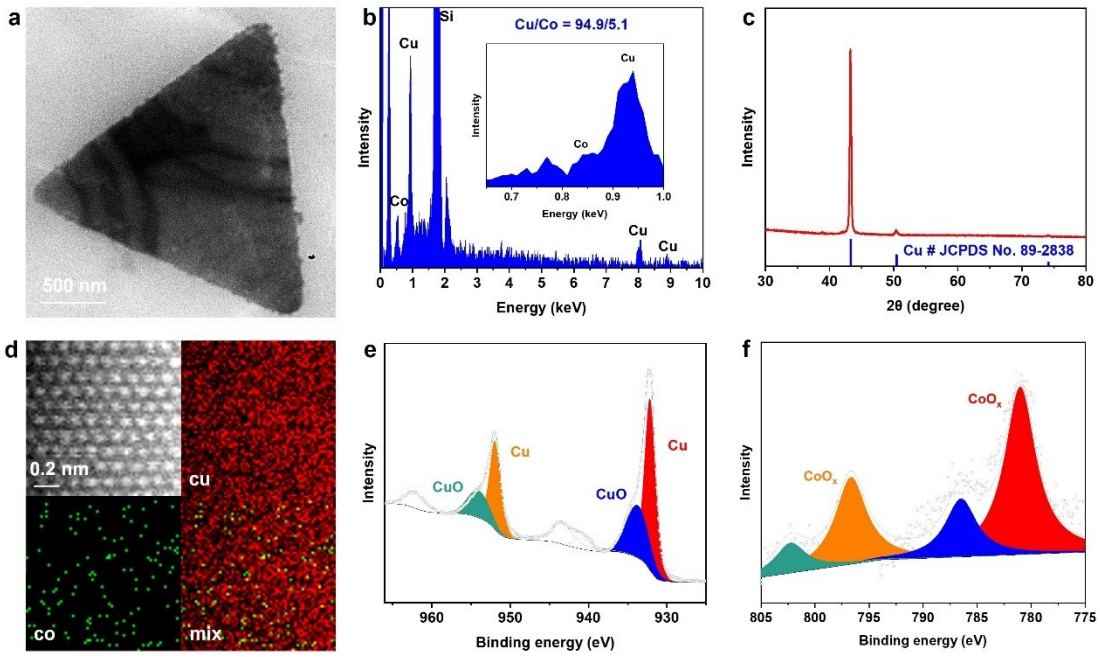

Fig. S15 (a) TEM image, (b) SEM-EDS, (c) PXRD pattern, (d) HADDF-STEM image with elemental mappings, (e) Cu 2p XPS spectra, and (f) Co 2p XPS spectra of $CuCo_1$ sheets after reaction.

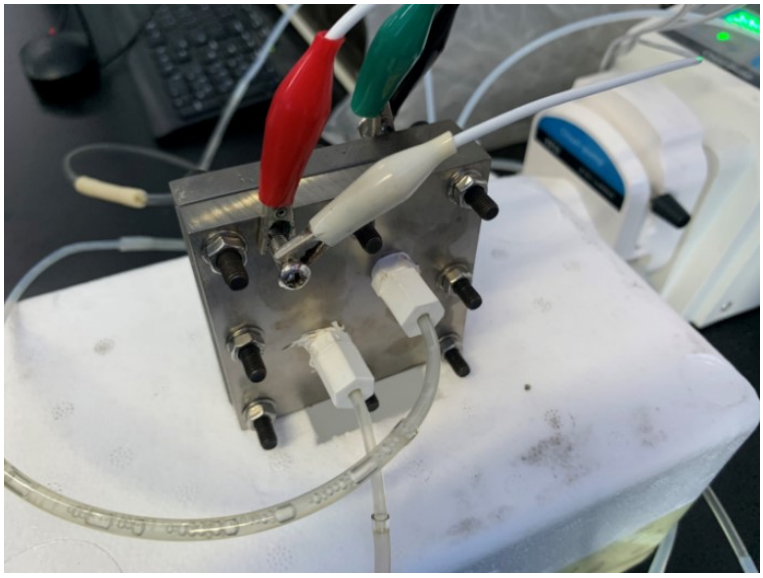

Fig. S16 Digital image of MEA electrolyzer.

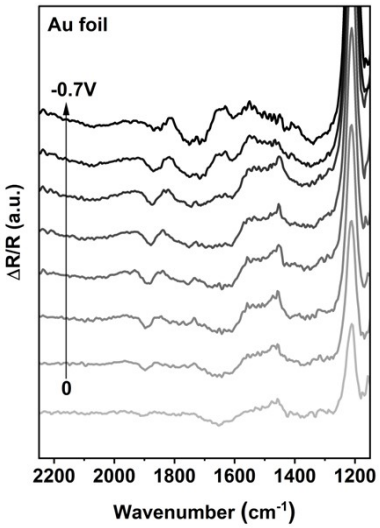

Fig. S17 *In situ* ATR-SEIRAS was obtained during chronopotentiometry in a potential window of 0 to –0.7 V versus RHE for the Au foil background.

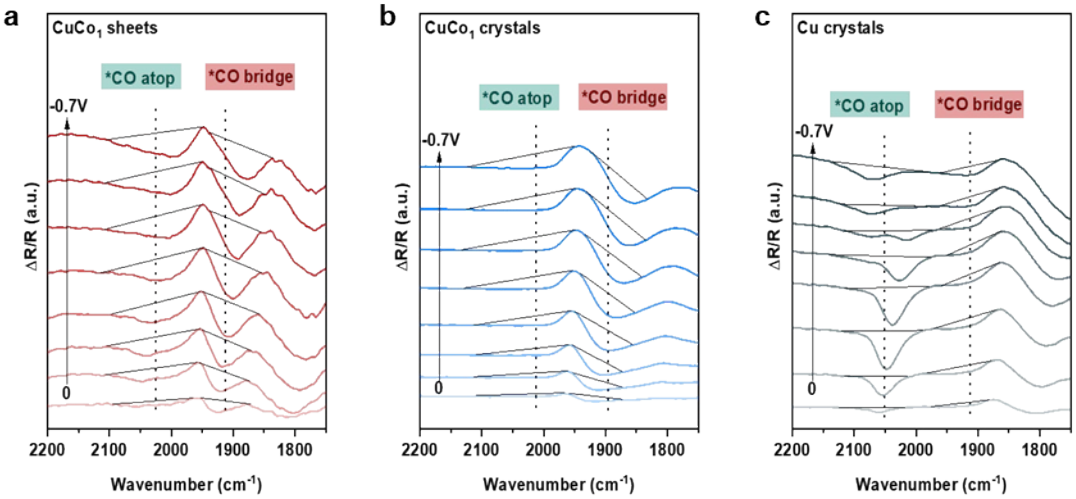

Fig. S18 *In situ* ATR-SEIRAS for $^{*}CO_{bridge}$ and $^{*}CO_{atop}$ peaks around 2100 to 1960 cm^{-1} and 1940 to 1840 cm^{-1} over (a) $CuCo_1$ sheets, (b) $CuCo_1$ crystals, and (c) Cu crystals. Baseline construction used end-point weighted-mode with 5% end point.

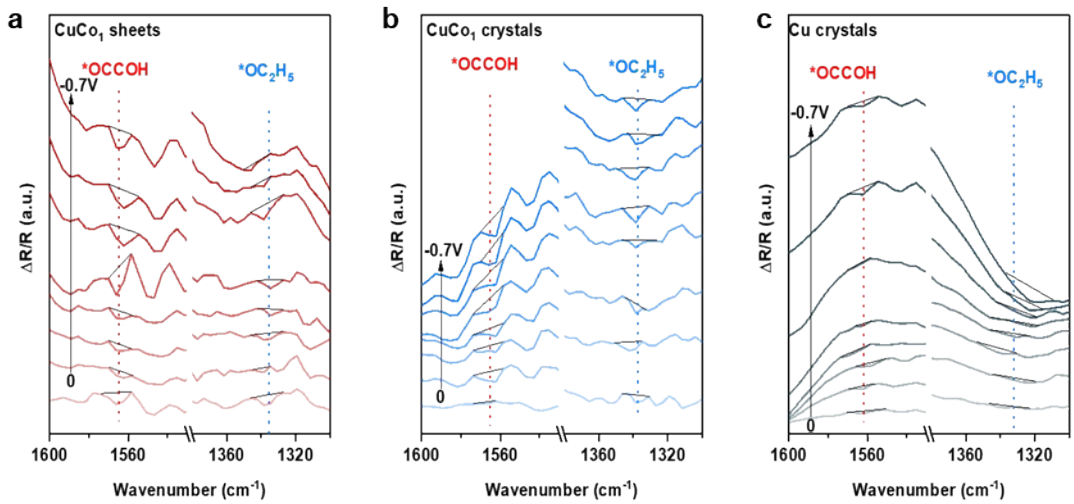

Fig. S19 *In situ* ATR-SEIRAS for $^{*}OCCOH$ and $^{*}OC_2H_5$ peaks around 1580 to 1550 cm^{-1} and 1350 to 1330 cm^{-1} over (a) $CuCo_1$ sheets, (b) $CuCo_1$ crystals, and (c) Cu crystals. Baseline construction used end-point weighted-mode with 5% end point.

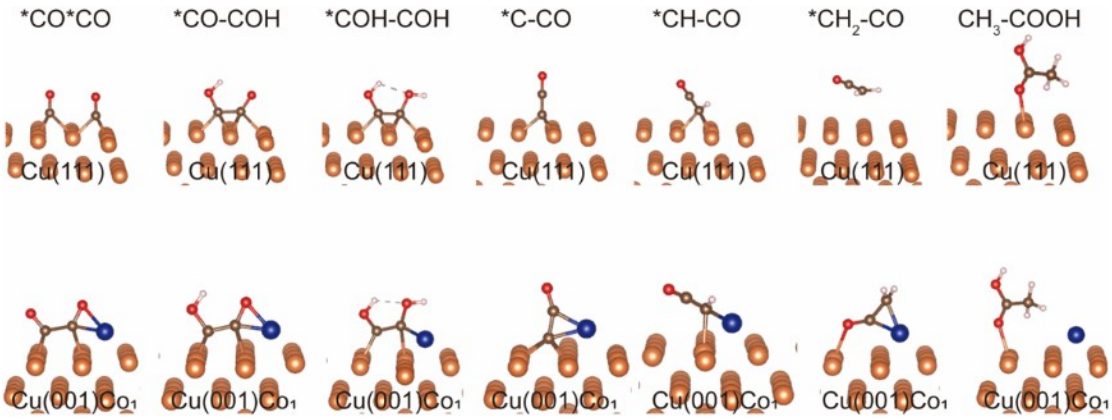

Fig. S20 Adsorption configuration of acetate intermediates on the ordered Cu(111) and Cu(001)Co_1 surface. Orange, cyan, brown, red and white spheres represent Cu, Co, C, O, and H atoms, respectively.

Table S1 Faradaic efficiencies for all products over $CuCo_1$ sheets in 1 M KOH at different current densities.

Current density	Faradaic efficiency (%)						
(mA cm^{-2})	H_2	C_2H_4	CH_4	Acetate	EtOH	n-PrOH	Total
100	15±2	2±2	2±1	52±3	23±5	6±1	99±1
200	9±3	1±1	1±1	55±4	22±4	5±1	94±2
300	9±1	2±2	2±2	59±2	16±0	4±1	92±2
400	8±1	3±1	2±2	61±2	22±2	6±1	101±5
500	10±2	0	0	63±4	19±1	8±3	100±3
600	7±2	0	0	72±3	18±3	4±1	101±2
700	9±1	2±0	1±0	48±4	25±4	9±5	93±3
800	24±2	0	1±1	47±5	15±2	6±2	94±7

Table S2 Comparison of CORR performance between $CuCo_1$ sheets and state-of-the-art Cu-type catalysts.

Catalyst	Pressure (MPa)	Electrolyte	Acetate faradaic efficiency (%)	Acetate current density (mA cm^{-2})	Stability (h)	Acetate formation rate (μmol s^{-1} cm^{-2})	Total loading (mg cm^{-2})	Mass normalized acetate formation rate (μmol s^{-1} mg^{-1})	Refs.
$CuCo_1$ sheets	**0.1**	**1 M KOH**	**71.8**	**430**	**500**	**1.11**	**0.44**	**2.53**	**This work**
CuPc	1	1 M KOH	84.2	421	102	1.09	2	0.55	Ref. 8
$CuAu_{1\%}$	0.1	1 M KOH	39	217	1	0.56	0.5	1.12	Ref. 9
Cu/Ag DA	1	5 M KOH	91	113	820	0.29	0.2	1.46	Ref. 10
Cu-CeO_2	0.1	1 M KOH	62.4	31.2	100	0.08	0.5	0.16	Ref. 11
Cu/C_3N_4	0.1	1 M KOH	62.8	188	20	0.49	0.3	1.62	Ref. 12
Cu@NH_2	0.1	1 M KOH	51.5	150	10	0.39	1	0.39	Ref. 13
Commercial Cu	0.1	5 M KOH	90	128	10	0.33	10	0.03	Ref. 14
$Cu_{49}Pd_{51}$	0.1	1 M KOH	68.7	142	30	0.37	1	0.37	Ref. 15
Cu/NC	0.1	1 M KOH	63	330	4	0.86	1	0.86	Ref. 16
Cu nanoparticle	0.1	2 M KOH	43.2	260	120	0.67	0.5	1.92	Ref. 17
CuPd	0.1	1 M KOH	70	425	500	1.1	0.5	2.20	Ref. 18
Cu_2O Cubes	0.1	1 M KOH	37.2	194	150	0.5	0.5	1.01	Ref. 19
N-Cu	0.1	2 M KOH	42	180	1	0.47	0.5	0.93	Ref. 20
$Cu_{0.9}Ni_{0.1}$	0.1	1 M KOH	47	93	3	0.24	0.34	0.71	Ref. 21
Cu nanosheets	0.1	2 M KOH	48	131	3	0.34	0.5	0.68	Ref. 1
Cu NC	0.1	0.5M $KHCO_3$	43	200	150	0.36	0.5	0.72	Ref. 22
Cu_2O-pyS	0.1	1 M KOH	62	380	100	0.35	1	0.35	Ref. 23
$CuPd_{0.6}$	0.1	2 M KOH	59.5	286	500	0.48	1	0.48	Ref. 24
LaF_3−Cu	0.1	1 M KOH	40.2	282	10	0.47	0.5	0.94	Ref. 25
Cu AEs	0.1	1 M KOH	70.2	225	140	0.58	0.5	1.16	Ref. 26

Table S3 Faradaic efficiencies for all products over $CuCo_1$ sheets during stability test in 2 M KOH MEA electrolyzer.

Time	Faradaic efficiency （%）					
h	H_2	CH_4	Acetate	EtOH	n-PrOH	Total
6.4	28.6	10.2	**45.7**	12.7	1.8	98.9
13.2	30.8	10.7	**46.3**	11.5	3.6	102.8
24.6	19.8	10.4	**52.4**	10.2	5.4	98.1
38.3	27.4	10.6	**47.5**	10.2	3.6	99.3
50.8	29.0	10.6	**50.6**	8.9	3.6	102.8
62.9	28.9	10.7	**50.0**	8.9	3.6	102.1
73.8	28.4	10.6	**45.7**	11.5	5.4	101.5
85.9	28.7	10.6	**49.4**	8.9	1.8	99.4
97.1	28.5	10.5	**48.8**	8.9	3.6	100.3
111.6	28.5	10.5	**51.8**	8.9	1.8	101.6
120.7	28.4	10.5	**50.6**	7.6	1.8	99.0
134.5	28.5	10.5	**48.8**	6.4	5.4	99.5
146.7	28.7	10.6	**51.2**	7.6	1.8	99.9
156.3	29.0	10.6	**46.3**	7.6	3.6	97.2
168.5	29.0	10.5	**42.7**	12.7	3.6	98.5
182.5	29.2	10.6	**46.3**	10.2	5.4	101.7
192.3	28.6	10.5	**45.7**	11.5	1.8	98.0
206.6	28.5	10.4	**48.1**	10.2	3.6	100.8
218.5	28.0	10.3	**48.8**	8.9	3.6	99.6
232.9	28.0	10.3	**50.0**	8.9	3.6	100.8
240.6	28.0	10.3	**46.3**	12.7	3.6	100.9
255.9	28.5	10.2	**47.5**	8.9	5.4	100.6
267.0	27.6	10.2	**48.1**	11.5	3.6	101.0
277.1	27.8	10.1	**45.1**	12.7	3.6	99.4
289.7	26.8	10.4	**45.7**	11.5	3.6	98.0
301.0	26.3	10.4	**50.6**	8.9	3.6	99.8
314.6	26.7	10.5	**51.2**	7.6	3.6	99.7
325.2	26.7	10.6	**48.8**	10.2	3.6	99.8
338.5	27.4	10.5	**45.1**	10.2	3.6	96.7
350.6	27.6	10.5	**46.9**	10.2	3.6	98.8
365.9	27.1	10.5	**45.7**	10.2	5.4	98.8
374.3	27.2	10.5	**50.0**	7.6	5.4	100.7
386.9	26.9	10.5	**48.8**	10.2	5.4	101.7
394.2	28.0	10.5	**50.6**	6.4	1.8	97.3
410.8	26.8	10.5	**46.9**	10.2	3.6	98.0
421.6	26.8	10.5	**48.1**	7.6	7.2	100.2
434.3	26.5	10.3	**45.7**	11.5	5.4	99.4
445.4	26.8	10.5	**45.1**	12.7	3.6	98.7
458.5	26.4	11.8	**45.7**	8.9	5.4	98.2
476.5	28.0	11.0	**46.3**	7.6	5.4	98.4
488.9	26.4	6.3	**46.9**	10.2	9.0	98.8
502.0	24.9	11.0	**45.1**	7.6	7.2	98.9

Table S4 Comparison of the detected intermediates and the corresponding band positions of *in situ* ATR-FTIR in the literatures.

Band center (cm^{-1})	**Band center (cm^{-1})**	**Assignment**	**Ref.**
This work	**Reported studies**		
2024	~1951–2094	$^{*}CO_{atop}$	*Nat. Commun.* **2023**, *14*, 340.
1890	~1806–1930	$^{*}CO_{bridge}$	*J. Am. Chem. Soc.* **2023**, *142*, 2857−2867.
~1566 and ~1168	~1584 and ~1191	$^{*}OCCOH$	*Nat. Commun.* **2022,** *13*, 3754.
~1268	~1235	$_{*}COH$	
~1427	~1370	$_{*}COOH$	*J. Am. Chem. Soc.* **2017**, *139*, 15664−15667.
~1334	~1338	$_{*}OC_2H_5$	*Nat. Commun.* **2022**, *13*, 3754.

Table S5 Adsorption configuration of acetate intermediates on the ordered Cu(111), Cu(001)Co_1, and Cu(111)Co_1 surface.

Gibbs free energy (eV)	Cu(111)	Cu(001)Co_1	Cu(111)Co_1
*CO−CO	0	0	0
*CO−COH	1.292263	-0.31926	-0.20502
*COH−COH	0.881668	0.650668	0.336838
*C−CO	0.534759	-0.04533	-0.37417
*CH−CO	0.550697	0.028357	-0.31231
$^*CH_2$−CO	0.835645	-0.70282	-0.98141
$^*CH_3$−COOH	-0.65734	0.89746	-1.10672

References

1. W. Luc, X. Fu, J. Shi, J.-J. Lv, M. Jouny, B. H. Ko, Y. Xu, Q. Tu, X. Hu, J. Wu, Q. Yue, Y. Liu, F. Jiao and Y. Kang, *Nat. Catal.*, 2019, **2**, 423-430.
2. Z.-M. Zhang, T. Wang, Y.-C. Cai, X.-Y. Li, J.-Y. Ye, Y. Zhou, N. Tian, Z.-Y. Zhou and S.-G. Sun, *Nat. Catal.*, 2024, **7**, 807-817.
3. G. Kresse and J. Hafner, *Phys. Rev. B*, 1994, **49**, 14251-14269.
4. G. Kresse and J. Furthmüller, *Phys. Rev. B*, 1996, **54**, 11169-11186.
5. P. E. Blöchl, *Phys. Rev. B*, 1994, **50**, 17953-17979.
6. G. Kresse and J. Furthmüller, *Comp. Mate. Sci.*, 1996, **6**, 15-50.
7. J. P. Perdew, K. Burke and M. Ernzerhof, *Phys. Rev. Lett.*, 1996, **77**, 3865-3868.
8. Y. Rong, T. Liu, J. Sang, R. Li, P. Wei, H. Li, A. Dong, L. Che, Q. Fu, D. Gao and G. Wang, *Angew. Chem. Int. Ed.*, 2023, **62**, e202309893.
9. Q. Sun, Y. Zhao, X. Tan, C. Jia, Z. Su, Q. Meyer, M. I. Ahmed and C. Zhao, *ACS Catal.*, 2023, **13**, 5689-5696.
10. J. Jin, J. Wicks, Q. Min, J. Li, Y. Hu, J. Ma, Y. Wang, Z. Jiang, Y. Xu, R. Lu, G. Si, P. Papangelakis, M. Shakouri, Q. Xiao, P. Ou, X. Wang, Z. Chen, W. Zhang, K. Yu, J. Song, X. Jiang, P. Qiu, Y. Lou, D. Wu, Y. Mao, A. Ozden, C. Wang, B. Y. Xia, X. Hu, V. P. Dravid, Y.-M. Yiu, T.-K. Sham, Z. Wang, D. Sinton, L. Mai, E. H. Sargent and Y. Pang, *Nature*, 2023, **617**, 724-729.
11. T. Yang, L. Lin, X. Lv, H. Yang, H. Feng, Z. Huang, J. Li, C.-W. Pao, Z. Hu, C. Zhan, Y. Xu, L.-S. Zheng, F. Jiao and X. Huang, *ACS Nano*, 2023, **17**, 8521-8529.
12. X. Yan, M. Zhang, Y. Chen, Y. Wu, R. Wu, Q. Wan, C. Liu, T. Zheng, R. Feng, J. Zhang, C. Chen, C. Xia, Q. Zhu, X. Sun, Q. Qian and B. Han, *Angew. Chem. Int. Ed.*, 2023, **62**, e202301507.
13. Y. Wang, J. Zhao, C. Cao, J. Ding, R. Wang, J. Zeng, J. Bao and B. Liu, *ACS Catal.*, 2023, **13**, 3532-3540.
14. S. Guo, Y. Liu, Y. Huang, H. Wang, E. Murphy, L. Delafontaine, J. L. Chen, I. V. Zenyuk and P. Atanassov, *ACS Energy Lett.*, 2023, **8**, 935-942.
15. H. Shen, Y. Wang, T. Chakraborty, G. Zhou, C. Wang, X. Fu, Y. Wang, J. Zhang, C. Li, F. Xu, L. Cao, T. Mueller and C. Wang, *ACS Catal.*, 2022, **12**, 5275-5283.
16. Z. Liu, J. Cao, B. Wu, L. Qian, A. Guan, C. Yang, X. Lv, L. Zhang and G. Zheng, *ACS Catal.*, 2022, **12**, 12555-12562.
17. S. Overa, B. S. Crandall, B. Shrimant, D. Tian, B. H. Ko, H. Shin, C. Bae and F. Jiao, *Nat. Catal.*, 2022, **5**, 738-745.
18. Y. Ji, Z. Chen, R. Wei, C. Yang, Y. Wang, J. Xu, H. Zhang, A. Guan, J. Chen, T.-K. Sham, J. Luo, Y. Yang, X. Xu and G. Zheng, *Nat. Catal.*, 2022, **5**, 251-258.
19. P. Zhu, C. Xia, C.-Y. Liu, K. Jiang, G. Gao, X. Zhang, Y. Xia, Y. Lei, H. N. Alshareef, T. P. Senftle and H. Wang, *Proc. Natl. Acad. Sci.*, 2020, **118**, e2010868118.
20. F. Ni, H. Yang, Y. Wen, H. Bai, L. Zhang, C. Cui, S. Li, S. He, T. Cheng, B. Zhang and H. Peng, *Sci. China Mater.*, 2020, **63**, 2606-2612.
21. C. Yang, B. H. Ko, S. Hwang, Z. Liu, Y. Yao, W. Luc, M. Cui, A. S. Malkani, T. Li, X. Wang, J. Dai, B. Xu, G. Wang, D. Su, F. Jiao and L. Hu, *Sci. Adv.*, 2020, **6**, eaaz6844.
22. P. Zhu, C. Xia, C.-Y. Liu, K. Jiang, G. Gao, X. Zhang, Y. Xia, Y. Lei, H. N. Alshareef, T. P. Senftle and H. Wang, *Proc. Natl. Acad. Sci.*, 2020, **118**, e2010868118.
23. J. Ding, F. Li, X. Ren, Y. Liu, Y. Li, Z. Shen, T. Wang, W. Wang, Y.-G. Wang, Y. Cui, H. Yang, T. Zhang and B. Liu, *Nat. Commun.*, 2024, **15**, 3641.
24. S. Li, G. Zhang, X. Ma, H. Gao, D. Fu, T. Wang, J. Zeng, Z.-J. Zhao, P. Zhang and J. Gong, *J. Am. Chem.Soc.*, 2024, **146**, 31927-31934.
25. Y. Zhao, Y. Li, J. Chen, B. Sun, L. Fan, J. Chen, Y. Xiao, H. Yang, D. Wang, J. Chen, X. Han, S. Xi, J. Zhang and L. Wang, *ACS Catal.*, 2024, **14**, 8366-8375.
26. L. Zhang, J. Feng, R. Wang, L. Wu, X. Song, X. Jin, X. Tan, S. Jia, X. Ma, L. Jing, Q. Zhu, X. Kang, J. Zhang, X. Sun and B. Han, *J. Am. Chem.Soc.*, 2024, **147**, 713-724.